WILEY-VCH

DOI: 10.1002/((please add manuscript number))
Article type: Communication

Substitutional Carbon-Modified Anatase TiO_2 Decahedral Plates Directly Derived from Titanium Oxalate Crystals via Topotactic Transition

Ping Niu,† Tingting Wu,† Lei Wen, Jun Tan, Yongqiang Yang, Shijian Zheng, Yan Liang, Feng Li, John TS Irvine, Gang Liu, Xiuliang Ma, Hui-Ming Cheng**

Dr P. Niu,† T. T. Wu,† Dr L. Wen, Prof. J. Tan, Dr. Y. Q. Yang, Prof. S. J. Zheng, Dr Y. Liang, Prof. F. Li, Prof. G. Liu, Prof. X. L. Ma, Prof. H. M. Cheng
Shenyang National Laboratory for Materials Science, Institute of Metal Research, Chinese Academy of Sciences, 72 Wenhua Road, Shenyang 110016, China

Prof. J. TS Irvine
School of Chemistry, University of St. Andrews, Fife, KY16 9ST, UK

Prof. G. Liu
School of Materials Science and Engineering, University of Science and Technology of China, 72 Wenhua Road, Shenyang 110016, China

Prof. H. M. Cheng
Low-Dimensional Material and Device Laboratory, Tsinghua-Berkeley Shenzhen Institute, Tsinghua University, 1001 Xueyuan Road, Shenzhen 518055, China

Prof. H. M. Cheng
Center of Excellence in Environmental Studies, King Abdulaziz University, Jeddah 21589, Saudi Arabia

† These authors contributed equally to this work.

E-mail: gangliu@imr.ac.cn (GL); cheng@imr.ac.cn (HMC)

Keywords: TiO_2, Topotactic, Carbon, Photocatalyst, Lithium

Abstract

Changing the composition and/or structure of some metal oxides at the atomic level can significantly improve their performance in different applications. Although many strategies have been developed, the introduction of heteroatoms, particularly anions to the internal part of metal oxide particles is still not adequate. Here, we demonstrated an effective strategy for directly preparing polycrystalline decahedral plates of substitutional carbon doped anatase TiO_2 from titanium(IV) oxalate by a thermally induced topotactic transition in an inert atmosphere. Because of the carbon concentration gradient introduced in side of the plates, the carbon doped TiO_2 ($TiO_{2-x}C_x$) shows an increased visible light absorption and a two orders of magnitude higher electrical conductivity than pure TiO_2. Consequently, it can be used as a photocatalyst and an active material for lithium storage, and shows a much superior activity in generating hydroxyl radicals under visible light and a greatly increased electrical specific capacity at high charge-discharge rates. The strategy developed could also be applicable to the atomic-scale modification of other metal oxides.

Changing the atomic composition and/or structure of metal oxide crystals to create favorable optical, electric, and magnetic, electrochemical properties for various applications has become important in the development of advanced functional materials.[1-8] Such changes can be achieved by introducing a small number of appropriate heteroatoms. The replacement of intrinsic atoms with the heteroatoms requires the breaking of the original metal-oxygen bonds and subsequently re-bonding the intrinsic atoms with heteroatoms by subsequent treatments that are widely used to obtain hetero-anion doped metal oxides (for example, annealing metal oxides in a gaseous ammonia atmosphere to achieve nitrogen doping that increases visible light absorption for photocatalysis or increases electrical conductivity for energy storage). Due to the nature of strong metal-oxygen bonds in most transition metal oxides such as TiO_2,[9] substitutional doping is usually thermodynamically unfavorable. Moreover, the long-range interaction of heteroatoms with intrinsic atoms to tailor the electronic structure of the oxides requires homogeneous introduction of the heteroatoms throughout the whole oxide particles.[9-11] The coupling of these two features, homogeneous and substitutional doping, is challenging to realize.

Topotactic transition is a unique process that produces various crystalline compounds simply by changing the crystallographic orientation(s) of the basic unit cells of the original materials, during which some nonmetallic elements such as H, F, and C are usually released. Using such a transition, many metal oxides,[12-17] particularly in the form of mesocrystals and faceted crystals, have been produced. For example, layered alkali or protonated titanate crystals have been topotactically converted into faceted anatase TiO_2 crystals by releasing alkali ions or protons into the solution under hydrothermal condition;[17] heating in air led to the topotactic conversion of NH_4TiOF_3 crystals into anatase TiO_2 mesocrystals with an obvious volume shrinkage due to the loss of fluorine and ammonia.[14] Considering the significance of some nonmetallic elements (B, C, N, S) with higher energy levels of *p* states than the O 2*p* states in changing the band structures of metal oxides,[1] intentionally retaining a small amount of these

elements in the raw materials may result in the generation of hetero-atom modified metal oxides with tailored properties during the topotactic transition process. In this study, as a demonstration, we used titanium(IV) oxalate decahedron crystals as the raw material to produce carbon-modified anatase TiO_2 decahedral plates by the topotactic transition in a controlled atmosphere. As a result of atomic carbon being located at oxygen lattice sites in the interior of the TiO_2 decahedral plates, the modified material shows increased visible light absorption and greatly increased electrical conductivity, and consequently a substantial increase in the photocatalytic generation of hydroxyl radicals and lithium ion storage ability at high discharge-charge rates. The strategy of using the topotactic transition process to modify TiO_2 at the atomic level could be applicable to other metal oxides.

The structure of titanium oxalate hydrate, $[Ti_2O_3(H_2O)_2](C_2O_4)\cdot H_2O$ (orthorhombic symmetry, space group *Cmca*, a=15.494 Å, b= 10.491 Å, c=9.700 Å) shown in the middle panel of **Figure 1,** consists of conjugated layers of corner-sharing TiO_6 octahedra interconnected by oxalate ions, and water molecules are separately located in the rhombus-like spaces.[18] Depending on the thermal treatment temperature, titanium oxalate hydrate can be topotactically converted into different polymorphs of TiO_2 (anatase, rutile or brookite) with TiO_6 octahedra as the building blocks.[19] The topotactic transition typically goes through the formation of several intermediates in the order of $[Ti_2O_3(H_2O)_2](C_2O_4)$, $Ti_2O_3(C_2O_4)$, $TiOCO_3$ and amorphous TiO_2 with the temperature increase before the emergence of a crystalline TiO_2 phase, accompanied by the release of water molecules and decomposition of the carbonate.[18] Such a transition process proceeding in air usually leads to the complete release of carbon species so that pure TiO_2 crystals are formed, as shown in the left panel of Fig. 1. It is anticipated that, if the conversion process were conducted in an inert atmosphere, carbon-modified TiO_2 crystals might be obtained by intentionally leaving some carbon atoms in the Ti-O-Ti framework, as shown in the right panel of Fig. 1.

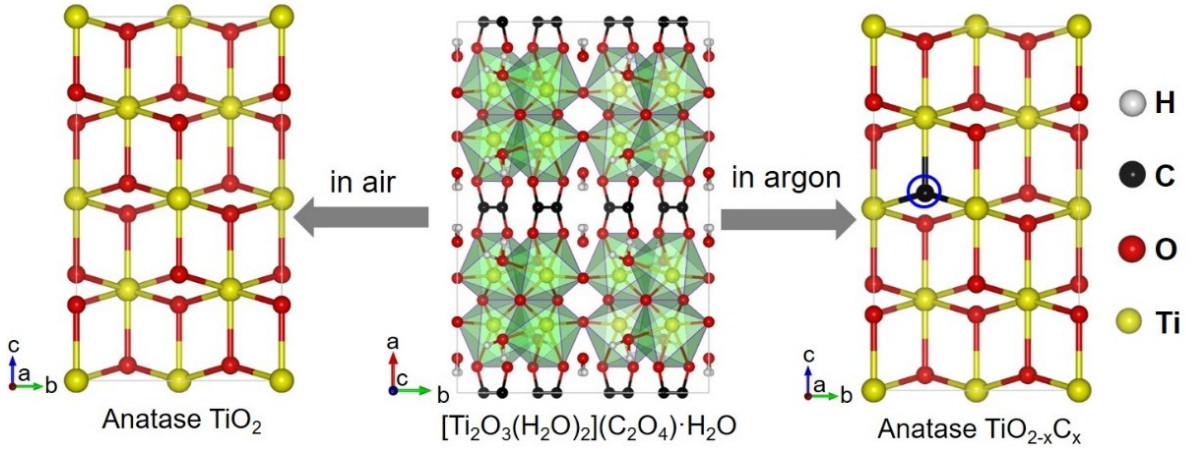

Figure 1 Schematic of the topotactic transition from titanium oxalate(IV) to anatase titanium dioxide. Atomic structure models of unit cells of (**the middle panel**) $[Ti_2O_3(H_2O)_2](C_2O_4)\cdot H_2O$, (**the left panel**) anatase TiO_2 and (**the right panel**) carbon-modified anatase $TiO_{2-x}C_x$. Anatase TiO_2 and $TiO_{2-x}C_x$ are topologically formed from $[Ti_2O_3(H_2O)_2](C_2O_4)\cdot H_2O$ by dehydration in atmospheres of air and argon, respectively.

Titanium oxalate hydrate crystals used for the topotactic transition were synthesized by a typical aqueous precipitation process with titanium oxysulfate as the precursor and oxalate as the ligand stabilizer of the titanium oxalate hydrate phase.[19] SEM images in **Figure 2a** and **b** show that the uniform particles of the titanium oxalate sample obtained have a plate-like decahedral shape. The typical length, width and thickness of these particles determined from transmission electron microscopy (TEM) image (**Figure S1**) are respectively > 2 μm, < 2 μm and around 700 nm. The strong and sharp peaks in X-ray diffraction (XRD) patterns of the sample in (**Figure S2**) are consistent with that for orthorhombic titanium oxalate, indicating the high crystallinity of the plate-like crystal. The formation of the plate-like decahedral shape is intrinsically controlled by the layered structure of titanium oxalate itself and driven by the minimization of total surface energy of the crystals in the reaction solution.[20] It is noted that some isolated nanoparticles are located on the plates largely because of the heterogeneous nucleation and post-growth of titanium oxalate nanoparticles on the homogeneous nucleation-

induced plates during the natural cooling process of the reaction solution from 90 ºC to room temperature used in this study. It is anticipated that some strategies like a fast cooling process might suppress such heterogeneous nucleation and post-growth for nanoparticles-free plates in further studies.

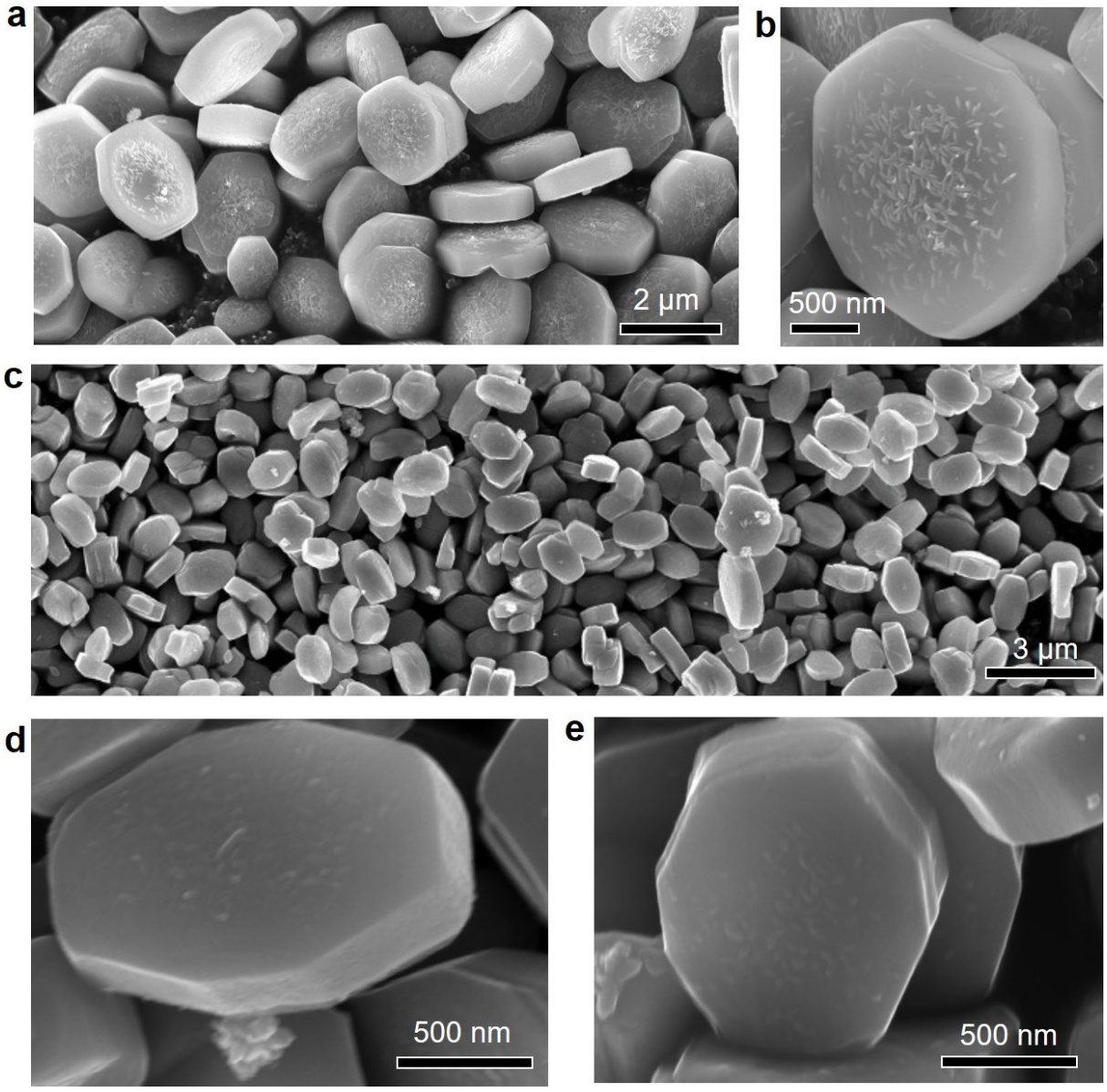

Figure 2 Morphology of titanium oxalate and anatase titanium dioxide crystals. Scanning electron microscopy (SEM) images of **(a, b)** $[Ti_2O_3(H_2O)_2](C_2O_4)\cdot H_2O$, **(c, d)** carbon-modified anatase $TiO_{2-x}C_x$ and (**e**) anatase TiO_2 samples derived from the $[Ti_2O_3(H_2O)_2](C_2O_4)\cdot H_2O$ raw material by dehydration at 550 ºC in atmospheres of air and argon, respectively. All samples show a uniform decahedra shape.

The topotactic transition of titanium oxalate crystals induced by thermal treatment leads to the formation of anatase TiO_2 crystals as indicated by the XRD patterns in **Figures S3** and **S4**, and this is independent of whether treatment atmosphere is air or argon. The derived TiO_2 and $TiO_{2-x}C_x$ crystals remain a similar shape of decahedral plates to that of the titanium oxalate crystals as shown in **Figs. 2**c-e. Comparison of the thickness of the titanium oxalate and $TiO_2/TiO_{2-x}C_x$ crystals shows a small volume shrinkage because of the release of oxalate ions and water molecules from the titanium oxalate crystals. Compared to the sharp XRD diffraction peaks of the titanium oxalate crystals, the much wider peaks of $TiO_2/TiO_{2-x}C_x$ suggest refinement of the crystal grains of the plates during the topotactic transition.

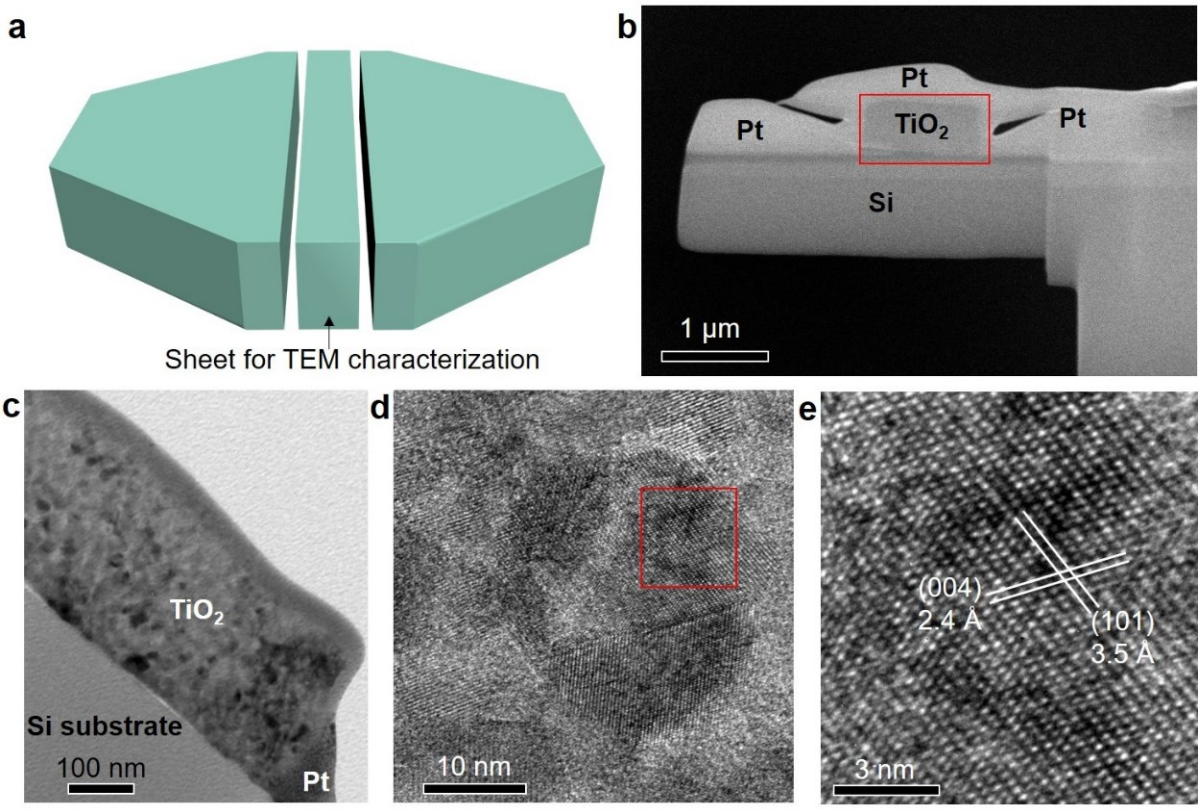

Figure 3 Microstructure characterization of a carbon-modified anatase TiO_2 decahedron. a, Schematic of cutting a slice of a carbon-modified anatase $TiO_{2-x}C_x$ sample supported on a silicon wafer substrate by the Focused Ion Beam technique. The middle rectangular sheet obtained after cutting was used as the sample for TEM characterization. **b,**

SEM image of the rectangular sheet cut from the $TiO_{2-x}C_x$ particle that is loaded on the silicon substrate by depositing a layer of platinum on the exposed surfaces of the particle. The red rectangle marks the newly exposed inner surface of the particle after cutting. **c,** Low-magnification TEM image of the $TiO_{2-x}C_x$ sheet after removing most of the top platinum layer in **b**. The incident electron beam for TEM characterization was perpendicular to the newly exposed surface of the sheet. **d,** High-magnification TEM image recorded from a typical region of the $TiO_{2-x}C_x$ sheet in **c**. **e,** Image of the lattice atoms enlarged from the local region of a primary particle in the area marked by the red rectangle in **d**.

To directly study the microstructure of the decahedral plate of the derived $TiO_{2-x}C_x$, a rectangular thin sheet with a thickness suitable for TEM characterization was cut from one particle, as demonstrated in **Figure 3a** and **b**. A low magnification TEM image showing different contrast at different regions of the sheet in **Figure 3c** suggests the polycrystalline nature of the sample, which is also confirmed by the electron diffraction ring patterns of the sample (**Figure S5**). The sheet consists of closely packed polyhedral nanoparticles with tens of nanometers in size. Despite the atomic carbon doping, these nanoparticles are highly crystalline as indicated by the clear lattice fringes. The measured lattice spacings of 3.5 and 2.4 Å are respectively assigned to the commonly observed (101) and (001) planes of anatase TiO_2 crystals. It suggests that the surface of these polyhedral nanoparticles in the decahedral plates probably consists of major low-energy {101} facets and minor high-energy {001} facets. The (001) surface with 100% unsatuated titanium and oxygen atoms plays an unique role in mediating photocatalysis and lithium storage of TiO_2.[20]

The presence of atomic carbon in the form of Ti-C bonds in anatase TiO_2 derived from titanium oxalate in an argon atmosphere was confirmed by X-ray photoelectron spectroscopy (XPS). The depth-dependent XPS spectra of the C 1*s* core electrons in **Figure 4a** show a gradual increase of the signal peak centered at around 282.1 eV with the increased sputtering

time, which is a typical value for the binding energy of C 1*s* core electrons of the carbon species in a Ti-C bond[21]. This result indicates that there is a gradient of substitutional carbon with its minimum concentration at the surface of the TiO_2 particles. Based on the XPS result, the atomic ratio of C to Ti in the bulk was estimated to be 9.8%. Due to the absence of the carbon dopant in the surface layer of particles, the XPS spectrum of Ti 2*p* states from the pristine surface of the $TiO_{2-x}C_x$ sample retains the typical feature of the Ti^{4+} oxidation state as that of TiO_2 (**Figure S6**). No XPS spectrum of the C 1*s* core electrons of the substitutional carbon for oxygen was detected from the TiO_2 sample derived from titanium oxalate in air (**Figure S7**).

The concentration gradient of carbon dopant plays a substantial role in improving both the visible light absorption and electrical conductivity of the TiO_2 plates. UV-visible absorption spectra (**Figure 4b**) shows that, compared to TiO_2, $TiO_{2-x}C_x$ has an additional visible light absorption band between 400 and 600 nm and also that the position of absorption edge has a redshift by 10 nm. These absorption features can be understood in terms of the energy level difference between the C 2*p* states and O 2*p* states and spatial distribution of the carbon dopant.[1] Due to the C 2*p* states having a higher energy level than the O 2*p* states, the substitution of carbon for oxygen in TiO_2 leads to either the formation of localized states above the valence band maximum, which results in an additional shoulder-like visible light absorption band, or a narrowing of the bandgap by mixing C 2*p* states with O 2*p* states dominated valence band, which causes the higher absorption edge. [11] It has been established that, at the atomic level the homogeneous distribution of various modifiers (i.e., dopants and defects)[10, 22, 23] to electronic structure in semiconductors is required for the bandgap narrowing while the surface distribution of the modifiers can lead to an additional shoulder-like absorption band. In the case of $TiO_{2-x}C_x$, the concentration gradient of carbon dopant can be considered a mixture of two so that both the bandgap narrowing and an additional shoulder-like visible light absorption band were observed. Considering the polycrystalline

nature of the decahedral plates, the homogeneity of the electronic structure characteristics of different plate surfaces was investigated by (CL) spectroscopy. Defect-related CL signals[24] recorded from three local regions on the basal and edge surfaces of two plates in **Figure 4c** are quite similar, suggesting the isotropic electronic features of the plates.

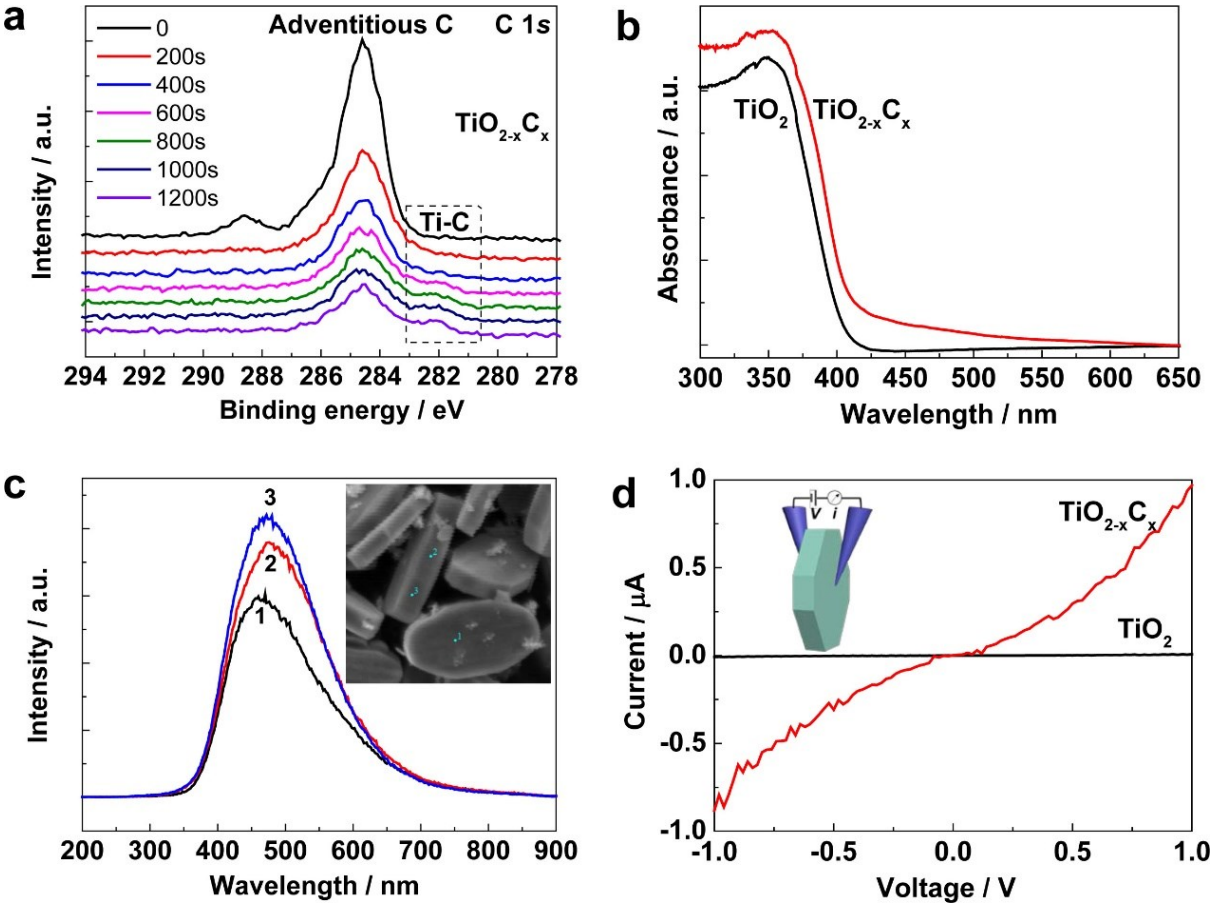

Figure 4 Carbon dopant-tailored optical and electrical properties of TiO_2. a, Sputtering time-dependent XPS spectra of the C 1*s* state recorded from sample $TiO_{2-x}C_x$. **b**, Diffuse reflectance UV-visible absorption spectra of samples TiO_2 and $TiO_{2-x}C_x$. **c**, Cathodoluminescence spectra recorded from three typical local regions of two plates of $TiO_{2-x}C_x$ at room temperature. **d**, Current-voltage curves measured from a TiO_2 or $TiO_{2-x}C_x$ particle. The inset is the schematic of measuring a particle with two tungsten probes, which was conducted in a scanning electron microscope.

The location of the atomic carbon dopant inside the plates greatly improves the electrical conductivity of $TiO_{2-x}C_x$. **Figure 4d** compares the current-voltage curves of a TiO_2 and $TiO_{2-x}C_x$ plate in a direction perpendicular to the basal surface. Although the $TiO_{2-x}C_x$ plate retains its typical semiconducting feature, its electrical conductivity is around two orders of magnitude higher than that of the TiO_2 plate (**Figure S8**). The conductivity improvement is attributed to the increased concentration of charge carriers for electrical conduction in the $TiO_{2-x}C_x$ plates as a result of the concomitant oxygen vacancies and related Ti^{3+} defects with the replacement of lattice O^{2-} with C^{4-} dopant. Comparison of electron spin resonance spectra of TiO_2 and $TiO_{2-x}C_x$ in **Figure S9** suggests the increase of oxygen vacancies with a signal at g = 2.000 and formation of possible (sub)surface-layer Ti^{3+} defects with complex signals (g = 1.893, 1.930, 1.995) in $TiO_{2-x}C_x$.[25, 26] These defects can also partially contribute to visible light absorption by forming some localized states in the gap.

The increased visible light absorption and increased electrical conduction mentioned above make the $TiO_{2-x}C_x$ sample an attractive material for photocatalysis and lithium ion storage. The generation of hydroxyl radicals (•OH) under visible light, which are an important active oxidative species for the degradation of organic pollutants,[27] was monitored to evaluate the photocatalytic activity of the $TiO_{2-x}C_x$ sample as a visible light photocatalyst. It is known that •OH radicals react with terephthalic acid (TA) to produce 2-hydroxy terephthalic acid (TAOH), emitting a unique photoluminescence (PL) signal at 426 nm.[28] Therefore, the PL spectra of TAOH generated by the visible light irradiation of $TiO_{2-x}C_x$ suspended in a TA aqueous solution were recorded. The obvious PL signals originating from TAOH in **Figure 5a** suggest that $TiO_{2-x}C_x$ is active in generating •OH radicals under visible light. The much superior activity of $TiO_{2-x}C_x$ to TiO_2 in **Figure 5b** is attributed to the increased visible light absorption. Moreover, the nearly linear increase of the PL signal at 426 nm indicates the good stability of $TiO_{2-x}C_x$ as a photocatalyst. It is proposed that the presence of carbon dopant in

the interior of the $TiO_{2-x}C_x$ prevents its oxidation and gives a good stability when exposed to an atmosphere containing oxygen and water.

Figure 5c and **d** compare the electrochemical lithium storage properties of $TiO_{2-x}C_x$ and TiO_2 anodes in lithium ion batteries with a similar thickness at different charge-discharge rates from 0.2 C to 15 C. Both anodes at the low rate of 0.2 C have a capacity of around 150 mA h g^{-1}. However, the $TiO_{2-x}C_x$ anode has a much higher lithium storage capacity than the TiO_2 anode at all other higher rates. Moreover, the capacity difference between the two anodes increases with increasing charge-discharge rates. In particular, the specific capacity of the $TiO_{2-x}C_x$ anode at the rate of 15 C is 2.5 times higher than that of the TiO_2 anode (79 *vs* 32 mA h g^{-1}). In addition to the greatly improved capacity at the high rates, the $TiO_{2-x}C_x$ anode has excellent cycling stability at both low and high rates as shown in Figure 5e. Moreover, $TiO_{2-x}C_x$ also shows a much higher lithium storage capacity at high rates than the reported {001} faceted anatase TiO_2 microspheres, {010} faceted anatase TiO_2 microrods and even N/S codoped anatase TiO_2 nanoparticles, as compared in **Table S1**.[29,30] All these results indicate the very promising lithium storage properties of $TiO_{2-x}C_x$.

The lithium storage process is intrinsically controlled by the balance between lithium ion transport and electron transport in the active materials, and these two parameters are affected by many factors including particle size, crystallinity, surface area, electrical conductivity, crystal facets, and also crystallographic orientations.[29-34] Most metal oxides used for lithium storage, like TiO_2 always suffer from low electrical conductivity because of their semiconducting nature so that their capacities at high charge-discharge rates are usually low. In this study, the most distinct physicochemical difference between the two TiO_2 samples lies in their electrical conductivity as indicated by Figure 4d. The significantly improved electrical conductivity of $TiO_{2-x}C_x$ definitely favors electron transport in the anode of $TiO_{2-x}C_x$. This suggestion is supported by the reduced Ohmic resistance (R_e, determined from the interconnection point between the left end of the semicircle and the X axis of the Nyquist

plots in Figure 5f, 12.1 Ω for $TiO_{2-x}C_x$ *vs* 20.7 Ω for TiO_2) of the cell with a $TiO_{2-x}C_x$ anode. On the other hand, comparison of the Nyquist plots shows a much smaller charge transfer resistance (R_{CT}, roughly estimated from the interconnection point between the semicircle and linear part of the Nyquist plots, 145.5 *vs* 474.9 Ω) between the electrode and the electrolyte in the cell with a $TiO_{2-x}C_x$ anode than that with the anode of TiO_2.

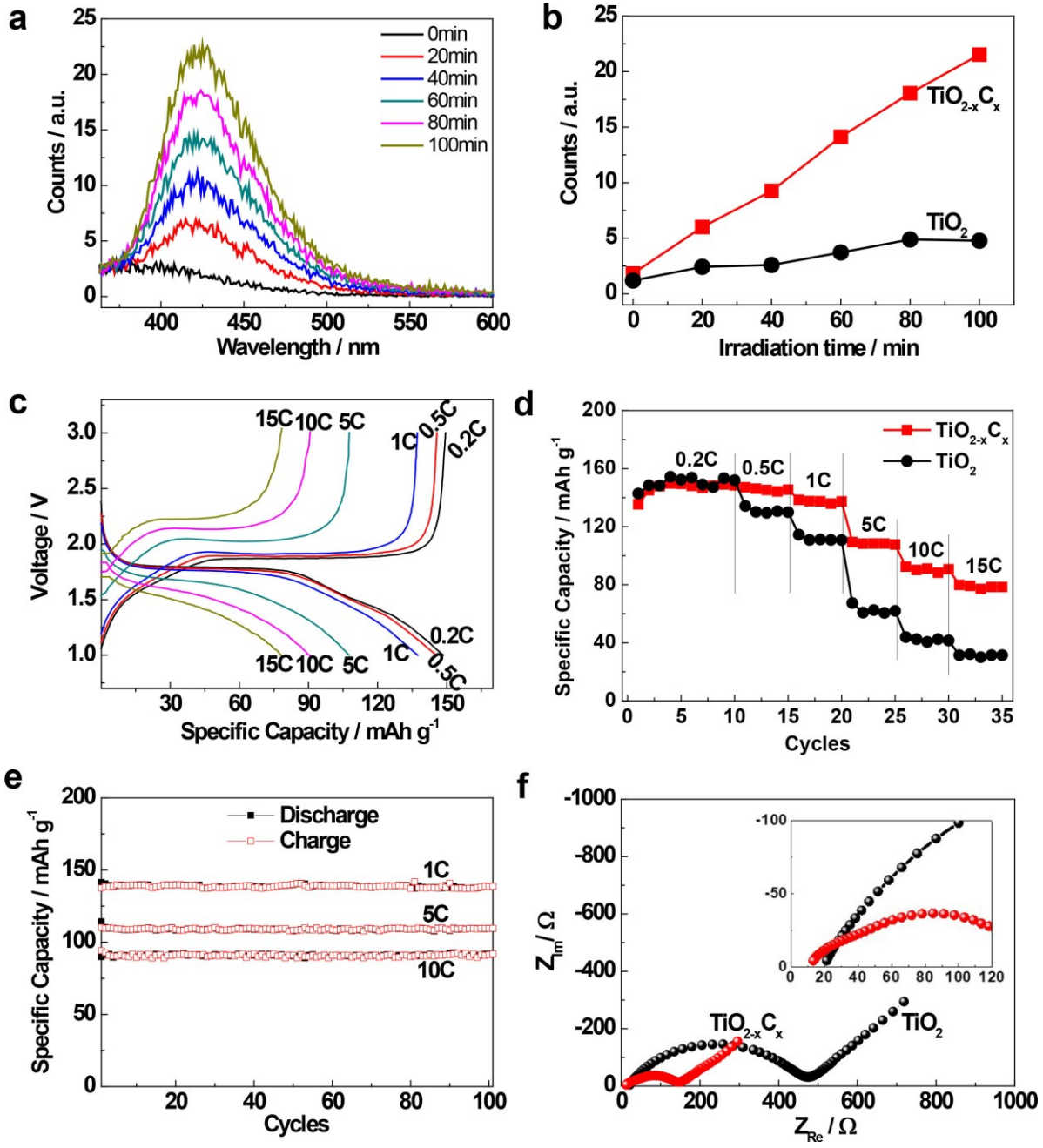

Figure 5 Photocatalytic activity and lithium ion storage capability. a, PL spectra of TAOH generated from $TiO_{2-x}C_x$ suspended in a terephthalic acid (TA) solution under visible

light irradiation (λ > 420 nm) for different irradiation times. **b,** Light irradiation time dependence of PL intensity at 426 nm of TAOH generated by $TiO_{2-x}C_x$ or TiO_2 photocatalyst under visible light irradiation. **c,** Galvanostatic charge–discharge curves of the $TiO_{2-x}C_x$ and TiO_2 anodes used in lithium ion batteries. **d**, Comparison of the specific capacity of $TiO_{2-x}C_x$ and TiO_2 anodes in lithium ion batteries at charge/discharge rates from 0.2 C to 15 C. **e**, Cycling stability of the $TiO_{2-x}C_x$ anode at 1 C, 5 C and 10 C. **f**, Nyquist plots of the $TiO_{2-x}C_x$ anode measured after the first cycle at 0.2 C in the charged state (3 V *vs* Li^+/Li).

It is important to understand the relationship between R_e and R_{CT} for understanding high-performance electrodes. The widely used strategy for addressing the shortcoming of the low electrical conductivity of metal oxides as active materials for lithium ion storage is coupling them with electrically conductive additives or substrates such as graphene or reduced graphene oxide.[35-38] Although the properties of the metal oxides in these hybrids are hardly changed, the R_{CT} of metal oxide/graphene based electrodes is significantly reduced with a decrease of Re. This result clearly indicates the positively strong correlation between Re and R_{CT} in anodes formed from hybrids of an active material and a conductive substrate.[39, 40] On the basis of the simultaneously reduced Re and R_{CT} of an anode containing only a single component ($TiO_{2-x}C_x$) with increased electrical conductivity shown in Figure 5f, the strong correlation between Re and R_{CT} is confirmed.

Finally, it is useful to highlight the advantage and significance of the topotactic transition developed in producing TiO_2 with tailored properties for photocatalysis and lithium storage in two aspects. The first aspect is the facile *in-situ* incorporation of *substitutional* carbon dopant in the bulk of TiO_2 for the improved visible light absorption and electrical conductivity that remains a challenge by conventional doping process. The location of carbon dopant in the bulk instead of surface layer of TiO_2 can prevent the dopants from oxidation by isolating the dopant from the environment. The second aspect is that the decahedral plates of $TiO_{2-x}C_x$ with

the length of over 2 μm are easy to recover from solution after photocatalysis reaction, and also lead to a much larger volume-energy-density than common nanoparticles in lithium ion batteries.

In summary, carbon-modified polycrystalline anatase TiO_2 decahedral plates consisting of nanocrystals tens of nanometers in size were prepared by the topotactic transition of titanium oxalate decahedron crystals in a controlled atmosphere of argon. As a result of intentional retaining of carbon from oxalate ions, a concentration gradient of atomic carbon in the form of Ti-C was formed in the interior of the $TiO_{2-x}C_x$ plates. Such a gradient causes an additional visible light absorption band together with a bandgap narrowing of $TiO_{2-x}C_x$, and significantly increases electrical conductivity. These features cause the $TiO_{2-x}C_x$ to be a good visible light photocatalyst for •OH radical generation and an excellent active material for lithium ion storage at high charge-discharge rates.

Experimental Section

Sample preparation: A sample of plates of titanium(IV) oxalate hydrate with the $[Ti_2O_3(H_2O)_2](C_2O_4)\cdot H_2O$ was synthesized using a modified procedure in the literature.[19] Briefly, 11.51 g of $TiOSO_4.xH_2O$ (MW: 159.93 g/mol) and 7.34 g of $Li_2C_2O_4$ (>99%) were sequentially dissolved in 80 mL of deionized water at room temperature, and the transparent aqueous solution obtained was kept in a water-bath at 90 ^oC for 6 h to allow the growth of titanium oxalate crystals. Finally, the white titanium oxalate powder was obtained by removing the solution containing dissolvable ions from the resultant white suspension, washing with deionized water several times, and drying at 80 ^oC in air.

A sample of $TiO_{2-x}C_x$ plates was prepared, first by heating the titanium oxalate sample at 550 ^oC in an argon atmosphere with an argon flow rate of 50 ml/min for 2 h. To decrease the generation of defects in the $TiO_{2-x}C_x$ during the toptactic transition in inert atmosphere, the

sample was further heated at 500 °C in air for 2 h. The TiO_2 reference sample was obtained by directly heating the titanium oxalate sample at 550 °C in air for 2 h.

Details for Material characterization, Photocatalysis activity measurement, and Lithium storage measurement are given in the Supporting Information.

Supporting Information

Supporting Information is available from the Wiley Online Library or from the authors.

Acknowledgements

The authors thank the Major Basic Research Program, Ministry of Science and Technology of China (2014CB239401), National Science Fund of China (Nos. 51422210, 21633009, 51561130157, 51521091), the Key Research Program of Frontier Sciences CAS (QYZDB-SSW-JSC039) for the financial support. G.L. is grateful for the award of a Newton Advanced Fellowship. We thank Professor Li-Chang Yin for drawing Figure 1 and Dr Ningdong Feng from Wuhan Institute of Physics and Mathematics, CAS for his valuable discussion on ESR spectra.

Received: ((will be filled in by the editorial staff))
Revised: ((will be filled in by the editorial staff))
Published online: ((will be filled in by the editorial staff))

[1] R. Asahi, T. Morikawa, T. Ohwaki, K. Aoki, Y. Taga, *Science* **2001**, *293*, 269.

[2] M. Freire, N. V. Kosova, C. Jordy, D. Chateigner, O. I. Lebedev, A. Maignan, V. Pralong, *Nat. Mater.* **2016**, *15*, 173.

[3] D. Neagu, G. Tsekouras, D. N. Miller, H. Menard, J. T. S. Irvine, *Nat. Chem.* **2013**, *5*, 916.

[4] S.-I. Ohkoshi, K. Imoto, A. Namai, S. Anan, M. Yoshikiyo, H. Tokoro, *J. Am. Chem. Soc.* **2017**, *139*, 13268-13271.

[5] Y. Ma, A. Kuc, T. Heine, *J. Am. Chem. Soc.* **2017**, *139*, 11694.

[6] X. Zhou, N. Liu, J. Schmidt, A. Kahnt, A. Osvet, S. Romeis, E. M. Zolnhofer, V. R. R. Marthala, D. M. Guldi, W. Peukert, M. Hartmann, K. Meyer, P. Schmuki, *Adv. Mater.* **2017**, *29*, 1604747.

[7] J. T. Mefford, W. G. Hardin, S. Dai, K. P. Johnston, K. J. Stevenson, *Nat. Mater.* **2014**, *13*, 726.

[8] F. Wu, M. Lv, X. Sun, Y. Xie, H. Chen, S. Ni, G. Liu, X. Xu, *Chemcatchem* **2016**, *8*, 615.

[9] G. Liu, L.-C. Yin, J. Wang, P. Niu, C. Zhen, Y. Xie, H.-M. Cheng, *Energy Environ. Sci.* **2012**, *5*, 9603.

[10] G. Liu, L. Wang, C. Sun, X. Yan, X. Wang, Z. Chen, S. C. Smith, H.-M. Cheng, G. Q. Lu, *Chem. Mater.* **2009**, *21*, 1266.

[11] G. Liu, L. Wang, H. G. Yang, H.-M. Cheng, G. Q. Lu, *J. Mater. Chem.* **2010**, *20*, 831.

[12] X. Zong, Z. Xing, H. Yu, Z. Chen, F. Tang, J. Zou, G. Q. Lu, L. Wang, *Chem. Commun.* **2011**, *47*, 11742.

[13] C. Z. Wen, Q. H. Hu, Y. N. Guo, X. Q. Gong, S. Z. Qiao, H. G. Yang, *Chem Commun.* **2011**, *47*, 6138.

[14] L. Zhou, D. Smyth-Boyle, P. O'Brien, *J. Am. Chem. Soc.* **2008**, *130*, 1309.

[15] P. Zhang, T. Tachikawa, M. Fujitsuka, T. Majima, *Chemsuschem* **2016**, *9*, 617.

[16] Z. Wang, B. Huang, Y. Dai, X. Zhu, Y. Liu, X. Zhang, X. Qin, *Crystengcomm* **2013**, *15*, 3436.

[17] J. Pan, X. Wu, L. Wang, G. Liu, G. Q. Lu, H.-M. Cheng, *Chem. Commun.* **2011**, *47*, 8361.

[18] C. Boudaren, T. Bataille, J. P. Auffredic, D. Louer, *Solid State Sci.* **2003**, *5*, 175.

[19] D. Dambournet, I. Belharouak, K. Amine, *Chem. Mater.* **2010**, *22*, 1173.

[20] G. Liu, H. G. Yang, J. Pan, Y. Q. Yang, G. Q. Lu, H. M. Cheng, *Chem. Rev.* **2014**, *114*, 9559.

[21] M. V. Kuznetsov, S. V. Borisov, O. P. Shepatkovskii, Y. G. Veksler, V. L. Kozhevnikov, *J. Surf. Inv. X-ray, Synchr. Neutr. Techn.* **2009**, *3*, 331.

[22] P. Niu, L.-C. Yin, Y.-Q. Yang, G. Liu, H.-M. Cheng, *Adv. Mater.* **2014**, *26*, 8046.

[23] Y. Kang, Y. Yang, L.-C. Yin, X. Kang, G. Liu, H.-M. Cheng, *Adv. Mater.* **2015**, *27*, 4572.

[24] M. Barberio, P. Barone, V. Pingitore, A. Bonanno, *Superlattice. Microst.* **2012**, *51*, 177.

[25] Y. Nakaoka, Y. Nosaka, *J. Photochem. Photobio. A-Chem.* **1997**, *110*, 299.

[26] M. Anpo, T. Shima, S. Kodama, Y. Kubokawa, *J. Phys. Chem.* **1987**, *91*, 4305.

[27] M. R. Hoffmann, S. T. Martin, W. Y. Choi, D. W. Bahnemann, *Chem. Rev.* **1995**, *95*, 69.

[28] T. Hirakawa, Y. Nosaka, *Langmuir* **2002**, *18*, 3247.

[29] G. Liu, L.-C. Yin, J. Pan, F. Li, L. Wen, C. Zhen, H.-M. Cheng, *Adv. Mater.* **2015**, *27*, 3507.

[30] W. Jiao, N. Li, L. Z. Wang, G. Liu, L. Wen, F. Li, H. M. Cheng, *Chem. Commun.* **2013**, 49, 3461.

[31] J. M. Tarascon, M. Armand, *Nature* **2001**, *414*, 359.

[32] P. Poizot, S. Laruelle, S. Grugeon, L. Dupont, J. M. Tarascon, *Nature* **2000**, *407*, 496.

[33] Y. Tang, Y. Zhang, X. Rui, D. Qi, Y. Luo, W. R. Leow, S. Chen, J. Guo, J. Wei, W. Li, J. Deng, Y. Lai, B. Ma, X. Chen, *Adv. Mater.* **2016**, *28*, 1567.

[34] Y. Tang, Y. Zhang, J. Deng, J. Wei, T. Hong Le, B. K. Chandran, Z. Dong, Z. Chen, X. Chen, *Adv. Mater.* **2014**, *26*, 6111.

[35] H. Wang, L.-F. Cui, Y. Yang, H. S. Casalongue, J. T. Robinson, Y. Liang, Y. Cui, H. Dai, *J. Am. Chem. Soc.* **2010**, *132*, 13978.

[36] Z.-S. Wu, W. Ren, L. Wen, L. Gao, J. Zhao, Z. Chen, G. Zhou, F. Li, H.-M. Cheng, *Acs Nano* **2010**, *4*, 3187.

[37] W. Zhou, J. Zhu, C. Cheng, J. Liu, H. Yang, C. Cong, C. Guan, X. Jia, H. J. Fan, Q.

Yan, C. M. Li, T. Yu, *Energy Environ. Sci.* **2011**, *4*, 4954.

[38] J. Luo, J. Liu, Z. Zeng, C. F. Ng, L. Ma, H. Zhang, J. Lin, Z. Shen, H. J. Fan, *Nano Lett.* **2013**, *13*, 6136.

[39] X.-Y. Shan, G. Zhou, L.-C. Yin, W.-J. Yu, F. Li, H.-M. Cheng, *J. Mater. Chem. A* **2014**, *2*, 17808.

[40] G. Zhou, D.-W. Wang, L.-C. Yin, N. Li, F. Li, H.-M. Cheng, *Acs Nano* **2012**, *6*, 3214.